HHS Public Access

Author manuscript

Magn Reson Med. Author manuscript; available in PMC 2022 August 15.

Published in final edited form as:

Magn Reson Med. 2021 April ; 85(4): 2145–2159. doi:10.1002/mrm.28537.

A Preclinical Study of Diffusion Weighted MR Image Contrast as an Early Indicator of Thermal Ablation

Steven P. Allen[1,*], **Francesco Prada**[2,3], **Zhiyuan Xu**[3], **Jeremy Gatesman**[4], **Xue Feng**[1], **Helen Sporkin**[1], **Yekaterina Gilbo**[1], **Sydney DeCleene**[1], **Kim Butts Pauly**[5], **Craig H. Meyer**[1,6]

[1]Department of Biomedical Engineering, University of Virginia, Charlottesville

[2]Department of Neurosurgery, Fondazione IRCCS Istituto Neurologico C. Besta, Milan

[3]Department of Neurosurgery, University of Virginia, Charlottesville

[4]Center for Comparative Medicine, University of Virginia, Charlottesville

[5]Department of Radiology, Stanford University, Stanford

[6]Department of Radiology, University of Virginia, Charlottesville

Abstract

Purpose: Intraoperative T2-weighted (T2-w) imaging unreliably captures image contrast specific to thermal ablation after transcranial MR-guided focused ultrasound surgery (T-MRgFUS), impeding dynamic imaging feedback. Using a porcine thalamotomy model, we test the unproven hypothesis that intraoperative diffusion weighted MRI (DWI) can improve dynamic feedback by detecting lesioning within 30 minutes of T-MRgFUS.

Methods: Twenty-five thermal lesions were formed in six porcine models using a clinical T-MRgFUS system. A novel diffusion-weighted pulse sequence monitored the formation of T2-w and DW lesion contrast after ablation. Using post-operative T2-w contrast to indicate lesioning, apparent intraoperative image contrasts and diffusion coefficients (ADCs) at each lesion site were computed as a function of time after ablation, observed peak temperature, and observed thermal dose. Lesion sizes segmented from imaging and thermometry were compared. Image reviewers estimated the time to emergence of lesion contrast. Intraoperative image contrasts were analyzed using receiver operator curves (ROCs).

Results: On average, the ADC at lesioned sites decreased within 5 minutes after ablation relative to control sites. In-plane lesion areas on intraoperative DW images varied from post-operative T2-w MRI and MR thermometry by 9.6 ± 9.7 mm^2 and -4.0 ± 7.1 mm^2, respectively. The 0.25, 0.5, and 0.75 quantiles of the earliest times of observed T2-w and DW lesion contrast were 10.7, 21.0 and 27.8 minutes and 3.7, 8.6 and 11.8 minutes, respectively. T2-w and DW contrasts and ADC values produced ROC areas-under-the-curve of 0.66, 0.80, and 0.74, respectively.

Conclusion: Intraoperative DWI can detect MRgFUS lesion formation in the brain within several minutes after treatment.

[*]Corresponding Author: 415 Lane Road, Charlottesville, VA, USA 22908, 434-924-5101, spa5c@virginia.edu.

Keywords

Diffusion MRI; HIFU; focused ultrasound; Thermal Ablation; lesioning; essential tremor

Introduction

Transcranial MR-guided focused ultrasound (T-MRgFUS) is a minimally invasive surgical method that alleviates symptoms related to essential tremor and tremor-dominant Parkinson's disease. The technique uses an electronically steerable transducer array to deposit 10-15 s duration bursts of acoustic energy into a precise volume of the patient's thalamus (1). Energy absorption induces highly localized thermal necrosis. When properly sited, the ablations produce a significant reduction in tremor symptoms (2-4). A multicenter pivotal trial has recently led to FDA approval for this surgery (5). T-MRgFUS is completely non-invasive and offers potential advantages in patient morbidity, recovery time, and procedural costs over invasive treatments such as deep brain stimulation (6,7). However, as pointed out in Boutet et al. (8), essential tremor symptom reductions after T-MRgFUS do not reach the same levels of efficacy as deep brain stimulation. There is a critical need to improve treatment efficacy and durability by ensuring that permanent tissue necrosis occurs within the entire ablation target.

Currently, surgeons rely on three intraoperative feedback mechanisms to control the location and shape of the ablated volume: (i) MR-thermometry, (ii) the patient's clinical response to sonication, and (iii) T2-weighted MRI (T2-w) (5). These data help the surgeon decide whether to continue sonicating the current target, to sonicate a new target, to change the sonication parameters, or to terminate the procedure. Decreased treatment efficacy is hypothesized to occur for three reasons: current MR thermometry methods coarsely sample the spatial and temporal heating trajectory (9); patient feedback can present ambiguous information about the durability of tremor reduction; and intraoperative T2-w imaging can poorly represent the final lesion size.

Meanwhile, if acquired four or more hours after ablation, post-operative T2-w MR images correlate well with cellular damage (10), clinical outcomes (8,11,12), and relevant treatment parameters such as thermal dose (13-16) and the 51 °C threshold (17). Intraoperative T2-w MRI, on the other hand, less effectively predicts treatment outcomes. Thermal lesions only develop T2 enhancement several tens of minutes after ablation (18). T2 contrast then continues to evolve over 24 hours (19), reducing the ability of intraoperative T2-w images to predict final lesion size. For example, Bond et al. indicated that T2 contrast varied by as much as 75% between 1 and 24 hours after ablation (17). At present, intraoperative T2-w MRI cannot resolve ambiguities posed by MR thermometry or patient feedback.

Diffusion-weighted imaging (DWI) has previously been proposed to provide earlier and more accurate detection of thermal ablation in the brain compared to T2-w MRI (19) —analogous to how DWI presents an earlier indicator of stroke. For example, thermal lesions introduce a broad array of cellular changes, including protein coagulation and cell swelling, that could possibly impact water diffusion at hyper acute time points (18,20,21). There is significant indirect evidence supporting this hypothesis. For example, many

researchers have found that DW contrast can always be observed several tens of minutes to hours after successful ablations in uterine fibroids (22,23), prostate (24,25), and brain (12,26-28). Post-operative diffusion tensor imaging indicates permanent changes to the thalamic diffusion model (27,29,30). Further studies indicated that DW contrast in prostate forms just a few minutes after exposure to an ablative thermal dose (31). Finally, Chazen et al. reported intraoperative DWI contrast midway through a clinical T-MRgFUS thalamotomy (32), which corresponds to a range between 10 and 60 minutes after reaching ablative temperatures. While these reports are promising, they do not test whether DWI contrast can be observed prior to the development of T2 lesion contrast or whether it can better predict lesion formation intraoperatively.

In this paper, we propose to test whether DWI can detect hyper acute thermal lesions using quantitative DWI measurements in a porcine T-MRgFUS thalamotomy model. We first present a novel, diffusion MRI pulse sequence and accompanying image reconstruction method appropriate for intraoperative diffusion imaging for T-MRgFUS. We then, holding post-operative T2-w imaging as an indicator for lesioning, compare the resulting intraoperative images from the porcine model to post-operative DW and T2-w images.

Methods

Animal Model

All animal experiments were conducted with the approval of the Institutional Animal Care and Use Committee of the University of Virginia. Experiments were conducted using six 15-28 kg porcine craniotomy models as described by Elias et al. (33). The void created by the missing skull was carefully filled with sterile water and the overlaying skin flap was kept in place using sutures. After successful craniotomy, each animal's head was positioned in a supine orientation at the focus of a 1024 element, 650 kHz, transducer system (ExAblate Neuro, INSIGHTEC, Haifa, Israel) and scanned inside a 3T MR scanner (GE MR750, General Electric, Waukesha, WI) using a custom-built, 25 cm diameter, circular, transmit-receive surface coil. The coil was constructed of copper tape and 8 equidistant MR-compatible capacitors (American Technical Ceramics, Huntington Station, NY) that rested on the lip of the transducer's open-bowl geometry. The coil's large diameter allowed the animal's head to protrude sufficiently far into the bowl to align the thalamus with the transducer focus. This setup is shown schematically in Figure 1.A.

The thalamus was localized by authors F.P. and Z.Y.X. by comparing T2-weighted MR images to a stereotaxic porcine atlas (34). Two to three targets in each hemisphere of the thalamus were located, for an average of 4.33 targets per animal and a total of 25 targets. For each animal, all targets were chosen on the same plane such that they could all simultaneously be visualized in a single MR slice. After sonication and imaging, the animals were removed from the transducer, transitioned to an 8-channel head coil in prone position, and subjected to further imaging. This transition took between 20-40 minutes. Upon completion, the animals were immediately euthanized. Because previous reports have established a strong correlation between post-operative T2-w imaging and tissue histology (12,18,20), no histology samples of the animal subjects were taken. Five out of six animals

presented normal heart rates, pulse oxidation values, and CO_2 saturation values over the course of the experiment. However, one of the six animals inadvertently expired 10 minutes after ablating the final target.

Sonication

Because of the small size of the animals and their corresponding craniotomies, a large portion of the transducer's surface area that would transmit into the remaining skull was deactivated, effectively increasing the transducer's f-number to 0.58 (focal length: 15 cm, aperture: 26 cm) and enlarging the focus to 2.4 x 4.1 mm. Treatment targets were first identified using stereotactic measures from the anterior-posterior commissure line and then sequentially subjected to two sonication schemes—targeting and treatment—with a 30 minute imaging session interleaved between each treatment. During the targeting phase, the selected ablation target was first subjected to several 13s sonications with acoustic powers of 20-40 W. During all targeting sonications, a 2D, Cartesian, multi-echo, gradient echo sequence was used to confirm sub-ablative temperature increases at the target. Thermometry sequence parameters were as follows. TR: 28 ms, field of view: 28 cm, slice thickness: 3mm, matrix size: 256x128 pixels, bandwidth: 35.7 kHz, echo times: 3.3, 8.0, 12.8, 17.6, and 22.4 ms, frame rate: 3.5 s.

After a successful targeting phase, the treatment phase proceeded in a manner similar to those conducted in clinical focused ultrasound treatments: the transmit power, and, if necessary, the sonication durations were increased over several successive sonications until the peak estimated temperature, as measured by MR thermometry, reached or exceeded a target temperature of 60°C. This temperature threshold strongly correlates with thermal coagulation in histology (20) and was chosen to enhance the likelihood of thermal lesioning. However, for several targets, peak temperatures at or above 60°C could not be achieved. A total of 9 of these sub-temperature targets were retained for study because either (5 targets) the peak temperatures fell within precision error (±1°C) of 60°C, or (4 targets), strong post-operative T2-W contrast and high thermal dose estimates indicated a high likelihood of lesioning. In several cases, one to three lesions were placed adjacent to each other to make the total treated volume large relative to the prescribed pixel size. Sonication parameters are presented in Table 1.

MRI Lesion Monitoring

After a successful treatment phase, the lesion was continuously monitored for 30 minutes using T2-w (for 4 out of 6 animals) and DW (for 6 out of 6 animals) imaging sequences. All sequences were programmed and implemented using the RTHawk framework (HeartVista, Menlo Park, CA). After imaging, the next target was selected and subjected to the same targeting-treatment-imaging protocol. Targeting, treating, and imaging one target consumed approximately 45-75 minutes. Transfer between the INSIGHTEC system to the RTHawk system included 1-2 minutes of cooling time, sequence download and safety checks, automatic and manual prescan calibrations, and scan prescription operations. For most treatment targets, these operations imposed a delay of 2-4 minutes between completion of sonication and the start of an intraoperative imaging session, as shown in Figure 1. However, in 4 out of 25 targets, a software error during transfer forced a scanner reset, resulting in

an approximately 10-30 minutes delay between ablation and the start of the intraoperative imaging session. For these lesions, data during these time points could not be collected and are not included in the analyses described below. Additionally, after all targets were identified in one animal, but prior to treatment, a control monitoring session was performed as a means to compute pre-ablation, baseline measures of image contrast and ADC values. Descriptions of the sequences used are presented below and specific sequence parameters are described in Table 2.

DW Imaging

DWI is inherently a low signal-to-noise (SNR) measurement. Large gradients sensitize the sequence to both eddy currents and vibrational and pulsatile motion. The transducer's construction, along with acoustic coupling water bath, introduced features that exacerbated these sensitivities, including a geometry incompatible with standard imaging coils, a conductive transducer surface that generates B1 RF standing waves, and eddy currents (35). Finally, motion in the water bath caused by strong vibrations induced by the imaging gradients could also pose a problem to image quality (36). In response, we constructed a custom, 25 cm transmit/receive surface coil that shifted the standing wave nodes, employed a twice-refocused, adiabatic spin echo scheme (37-39), and prescribed the selected slice to intersect with as little of the water bath as possible.

The strong eddy currents, potential corruption by the water bath, and B1 inhomogeneities precluded us from using the single-shot DW-EPI method that is standard in many diffusion studies in the brain. Multi-shot diffusion imaging methods were appealing because they could maintain a large field of view and relatively high spatial resolution. Our implementation consisted of a multi-slice, self-navigated spiral sequence (40). The spiral sequence employed a retraced readout to reduce image blur (41,42), and a twice refocused, adiabatic RF pulsing scheme to reduce both eddy currents and B1 inhomogeneity (37,39,43). Fat suppression was accomplished using a spectral-spatial RF excitation pulse (44). A schematic of the sequence is shown in Figure 1.B. Bloch simulations indicated that, with a TR of 1.5 s and a T1 of 1.3 s, non-selective adiabatic refocusing pulses would cause approximately 10% losses in signal magnitude relative to using slice-selective refocusing pulses when fewer than 4 slices were excited. The variable-density spiral was designed to vary the k-space distance between spiral arms according to the following exponential function

$$\frac{1}{spacing} = b + (a - b)e^{-\frac{fk}{a-b}} \quad (1)$$

Where a, b, and f are the desired imaging field of view, the desired imaging field of view at the edges of k-space, and the transition rate between the two sampling schemes, respectively. The resulting k-space trajectory is shown in Figure 1.C. To account for T2 shine-through, the sequence was also repeated with the diffusion encoding gradients disabled. These and all other data acquisition parameters are displayed in Table 2.

Work by Mazarolle et al. (30) indicated that, at 24 hours post ablation, the diffusion tensor changes most dramatically along the fiber's presumed axial direction. Therefore, in our study, all but two targets were imaged with the diffusion encoding gradients played in the posterior-anterior direction. The diffusion encoding gradients for the remaining two lesions were played in the superior-inferior direction.

T2-w Imaging

In four out of six animals, a T2-w imaging sequence was interleaved with the diffusion imaging sequence described above in the pattern shown in Figure 1.D. This sequence used the same adiabatic twice-refocusing scheme as the diffusion imaging sequence but lacked diffusion encoding gradients and employed a 90 ms echo time. Finally, because T2-w images do not require oversampled navigators at the center of k-space to correct for motion, a constant density spiral was used to sample k-space, reducing the number of interleaves per image to 40% of that used in the diffusion sequence.

Post-Operative Imaging

Post-operative imaging was completed using an 8-channel head coil and stock sequences provided by the scanner manufacturer. T2-w imaging was obtained using a 3D fast-spin-echo sequence (45) (TE/TR: 98 ms/3 s; echo train length: 130, field of view: 160x160x140 mm, matrix size: 256 x 256x 128; bandwidth: 244 kHz, acquisition time: 13 min). DW imaging was obtained using a single shot, DW-EPI sequence (TE/TR: 70 ms/ 8s; Field of View: 160 x 160 cm; matrix size: 128 x 128 x 22; slice width: 4 mm; slice spacing: 0.5 mm; bandwidth: 250 kHz; acceleration factor: 2; b values 0 and 1000; number of directions: 25). Slices corresponding to the treatment plane were retained for further analysis. Due to the sequential nature of the experiment, lesions were imaged between 1-5 hours after ablation and were assumed, by this time point, to produce visible T2-w contrast.

Image Reconstruction and Motion Artifact Correction

All image reconstruction and analyses were performed using custom scripts written in MATLAB (The MathWorks, Natick, MA). Motion navigators were extracted from each interleave of the spiral, multi-shot diffusion data by first convolving the sampled k-space data onto a Cartesian grid (46) and then windowing the resulting k-space data with a circularly symmetric, 2D, Gaussian window with a standard deviation of 3 pixels. The windowed k-space data were then converted into low resolution images via a Fourier transform. To reduce aliasing, the navigators produced by the spiral-in and spiral-out portions of each interleave were averaged together. The phase of the resulting images were then input into a single-channel adaptation of the iterative reconstruction method described by Liu et al. (47). This algorithm, implemented in the Michigan Image Reconstruction Toolbox (available at https://web.eecs.umich.edu/~fessler/code/index.html, downloaded September 18, 2017), was used to reconstruct images acquired at each time point after sonication. After reconstruction, the resulting images were subjected to a semi-automatic deblurring algorithm (42).

The reconstruction used a number of parameters, including center frequency, linear off resonance, number of iterations, and anisotropic delays. For reasons discussed later, these

parameters varied a great deal between monitoring sessions and were not always correctly estimated during prescan. For each series of images acquired after a successful thermal ablation, author S.P.A. manually tuned these parameters to provide the best lesion contrast and sharpest delineation of the brain's midline.

Semi-Quantitative Analysis

The visibility of both T2-w and DW contrasts at time points less than 35 minutes after sonication were semi-quantitatively assessed by having authors YKG, HS, and SD, who were unaware of the location and treatment order of each target, review a randomized stream of all intraoperative T2-w and DW images and identify the number of lesions visible in each image. Assuming previously treated targets displayed definite image contrast, the most recently sonicated target was assumed to be visible when the image viewer correctly identified the total number of treated targets in a given image plane. The earliest time points two or more reviewers correctly identified targets was labeled time to consensus detection and subjected to a Wilcoxon signed rank test. The null hypothesis that T2-w and DW-produced times to consensus detection sampled populations with identical medians was rejected if the p-value decreased below 0.05. To measure the size of each lesion, the same authors manually segmented the lesions on both intraoperative and post-operative images. Only image pixels labeled by two or more reviewers were retained as a part of the segmented lesion.

Quantitative Analysis

In the reconstructed images, regions of interest (ROI's) were selected about each lesion by manually identifying the center-most pixel of each lesion as it appeared on diffusion-weighted scans taken 30 minutes after ablation and then selecting a 3x3 pixel grid about this point. Both DW and T2-w images maintained identical scan prescriptions, facilitating registration. A control ROI was also selected in the grey matter of the cortex where no significant heat deposition was observed. For every acquired image, the magnitude of the MR signal at each target was estimated by first averaging the complex-valued MR data over this grid and then taking the magnitude of the result. The control ROI was also used to correct for magnetic field drifts, which could cause the signal magnitude of an ROI to change relative to the control session. This was done by first estimating the average signal magnitude differences in the control ROI between the baseline monitoring session and each subsequent monitoring session and then subtracting this difference from the appropriate ROI magnitude estimates. No attempt was made to remove signal bias caused by the magnitude operation as described by Gubjartson and Patz (48) and Miller and Joseph (49) because we found non-negligible levels of aliased signal in regions outside the transducer. The ADC of each ROI was computed using the standard scaled logarithm of the ratio of images acquired with different b-values. Finally, to better test our hypothesis, ROI's of any target acquired more than 35 minutes after final sonication of that target were discarded.

In total, each target produced three metrics: T2-w and DW magnitudes and an ADC estimate. These three metrics were converted to z-scores for easier comparison. First, the means and standard deviations of each metric were estimated by, respectively, averaging the magnitudes and computing the through-time standard deviation of the ROIs observed

during the baseline monitoring sessions. The resulting mean values were then subtracted from the ADC's and DW and T2-w signal magnitudes of each ROI, and the total difference was divided by the baseline standard deviation. Under this methodology, the resulting z-scores for the DW and T2-w ROI's were equivalent to signed contrast-to-noise calculations. To facilitate significance testing, the z-scores were binned into six groups of consecutive five minute increments after ablation. The binned groups were subjected to a Wilcoxon signed rank test of the null hypothesis that the z-scores sampled a zero-median population. Applying Bonferroni correction, the null hypothesis was rejected if the p-value decreased below 0.05/6 = 0.0083. Finally, because imaging sessions were interleaved between sequential treatments, many z-scores were derived from targets that had not yet been ablated. These were used to test the false positive rate of any lesion detection metric. Therefore, receiver operator characteristic (ROC) curves were calculated by using a series of z-score values as lesion detection thresholds for the ADC, DW, and T2-w ROI's, and then computing the resulting false positive and true positive rates.

Results

Image Quality

Different factors influenced the quality of the intraoperative DW images. For example, the transducer combined with the water bath to form a RF standing wave, introducing severe through-plane RF inhomogeneity. The standing wave node was 1-5 cm from the imaging plane, with larger pigs pushing the node closer to the imaging plane. While the dual, adiabatic refocusing pulses were able to partially mitigate this effect, the large slice width combined with inhomogeneous excitation produced through-plane blurring, which can be observed among all subjects. Further, image quality was greatly influenced by the water bath through several pathways: in addition to vibrating during the diffusion-encoding sequence and imposing a large field of view, the water bath, with a very long T1, skewed the RTHawk system's prescan calibration to favor accurate RF excitation flip angles in the water bath, destabilized the gradient delay calibrations, and de-optimized the receiver gain calibrations.

The destabilization of the prescan algorithm caused by these effects contributed to variable shim estimations, necessitating the need for manual calibration at each monitoring instance as well as further correction, on a case-by-case basis, during image reconstruction. Further, cerebral pulsatile motion artifacts appeared to increase with both the size of the animal as well as tension of the skin flap covering the craniotomy. A looser skin flap possibly allowed the skin-water interface to dampen pulsatile motion generated by each cardiac pulse. Fortunately, most motion-induced phase errors remained at sufficiently low spatial frequencies to be captured by the navigators and removed from the images. However, water vibrations sometimes imposed high frequency phase content, which could not always be removed. In each case, we found a continuum of tradeoffs between the size of the navigator window, the removal of motion artifact, and the degree of incoherent aliasing caused by the removal of aliased image phase. Supporting Information Figure S1 displays examples of the effects of navigator size and center frequency on image reconstruction. Meanwhile, Supporting Information Figures S2-13 display intraoperative images from all subjects. Residual pulsatile motion artifacts can be seen in Supporting Inforamtion

Figures S7 and S11 and aliasing from strong water bath vibrations are especially apparent Supporting Information Figures S8-9. Finally, the effects of image variability can be further demonstrated by comparing the ADC values of lesion ROI's obtained by the post-operative EPI sequence and those obtained by the custom intra-operative sequence. The mean and standard deviation of the differences between these two values were found to be $-0.95 \pm 3.25 \times 10^{-4}$ mm^2 s^{-1}.

Post-Operative Imaging

A total of 23 out of 25 targets readily displayed contrast on post-operative T2-w and DW imaging. The final two lesions in subject 6, which expired 10 minutes into the final monitoring session, could not be observed in post-operative imaging. Targets where only a single lesion was deposited displayed ring-like structures characteristic of post-operative T2-w imaging of thermal lesions (12,20). Targets with multiple lesions spaced together presented more complex structures. The 24 observable lesions displayed in-plane and through-slice dimensions of 23.2 ± 11 mm^2 and 10.0 ± 3.3 mm, respectively.

Comparison Between Intra-Operative and Post-Operative Imaging

When observed intraoperatively, lesions displayed hyper-intense contrast on both intraoperative T2-w and DW images. Ring structures were not visible. Image reviewers were able to segment 11 and 22 of the 25 lesions using intraoperative T2-w contrast and DW contrast, respectively. The lesion areas segmented on post-operative T2-w images minus the areas on the successfully segmented intraoperative DW and T2-w images were 9.6 ± 9.7 mm^2 and 16.1 ± 8.1 mm^2, respectively. Meanwhile, the lesion areas segmented on intraoperative DW and T2-w images minus the dose areas reported in Table 1 were -4.0 ± 7.1 mm^2 and 2.0 ± 7.1 mm^2, respectively. These large differences are discussed later in this paper.

Example intraoperative images from subject 5 are shown on the top row of Figure 2, with T2-w and DW images acquired less than 8 minutes after ablating the 4^{th} and final lesion in the animal. By this time point, the prior 3 lesions have had 1-3 hours to develop strong T2-w and DW contrast. The 4^{th} lesion presents observable intraoperative DW contrast and remains much smaller and harder to distinguish on T2-w imaging. Post-operative T2-w and DW images are displayed on the bottom row of Figure 2. At this point all lesions have had 1-4 hours to develop image contrast and are quite visible. The relative sizes and locations of all 4 lesions in the post-operative images appear consistent with the intraoperative images.

Time to Consensus Detection

Image reviewers were able to identify the correct number of sonicated lesions for 9 and 16 targets using intraoperative T2-w and DW images, respectively. The majority of identifiable lesions could be found at earlier time points on DW images than T2-w images. The times to consensus detection for observed targets produced 0.25, 0.5, and 0.75 quantiles of 10.7, 21.0 and 27.8 minutes and 3.7, 8.6 and 11.8 minutes for T2-w and DW images, respectively. These distributions are displayed in Figure 3 as violin plots. The Wilcoxon rank test produced a p-value of 0.002.

ADC Estimates

Example ADC maps from subject 6 are displayed in Figure 4. To reduce aliasing artifacts, these maps were computed from the average of the first two images acquired after a successful treatment phase with b = 0 and b = 815 s mm^{-2}. Ablation targets are indicated by white arrows. Lesions 1 and 3-4 show a decrease in ADC relative to baseline. Lesion 2 does not display an immediate decrease in ADC.

The T2-w, DW, and ADC z-scores for both target and control ROIs are displayed in Figure 5. Statistically significant data at the 0.0083 level are marked by an asterisk. The majority of DW z-scores acquired immediately after ablation display more pronounced contrast relative to the corresponding T2-w z-scores. This difference increases with time after ablation. Meanwhile, a small minority of lesions display either an increase in ADC or no observable change in ADC while the majority display a z-score between −1 and −5. For example, a z-score of zero indicates no change in the ADC between baseline and treatment monitoring sessions. Z-scores with a low magnitude indicate a small effect size relative to the native standard deviation of the metric. Finally, negative z-scores indicate that the ADC decreased between the baseline and treatment monitoring sessions, which would be consistent with our hypothesis. The control ROI's display an increase in ADC between the baseline and treatment monitoring sessions, which may be either physiologic or a result of residual scanner drift.

Comparison with Temperature Metrics

Figure 6 plots the ADC z-scores used for ROC analysis against both the peak temperatures and the thermal doses observed by MR thermometry. Pearson coefficients of the correlation between the temperature metrics and the z-scores are also presented in the corner of each plot. As in Figure 5, the plots show how the range of variations in the z-scores is small enough to detect changes between untreated and treated locations. However, the small Pearson coefficients suggest that possible linear relationships between the z-scores and temperature metrics are not easily observed in this study.

ROC Analysis

Figure 7 displays the resulting ROC curves for a variety of T2-w, DW, and ADC z-score classification thresholds. The solid black line with unity slope indicates classification accuracy equivalent to random chance. The figure demonstrates that classification thresholds using DW and ADC z-scores produce lower false positive rates than T2-w z-scores. The resulting areas under the curve, which equal the probabilities that a treated target will produce a larger magnitude z-score than an untreated target, are 0.66, 0.80, and 0.74 for the T2-w, DW, and ADC z-scores, respectively. Finally, the optimal thresholds associated with these points were -1.5, -1, and -1.1, respectively.

Discussion

The results presented here support the hypothesis that intraoperative DWI can detect thermal lesioning at hyper acute time points when T2-w contrast has yet to fully develop. Image reviewers found 75% of lesions to show DW image contrast within 12 minutes after

ablation. At all post-ablation time points, we observed a decrease in the average estimated ADC z-score of the treatment targets relative to pre-ablation time points. Meanwhile the ADC's of the control regions did not similarly decrease, contraindicating the possibility of confounds such as global field drifts or a systemic decrease in ADC values.

This study also provides some assessment of the utility of the early information provided by intraoperative DWI. For example, the ROC curves in Figure 7 suggest that DWI presents a higher likelihood, relative to T2-w imaging, of displaying enhanced contrast after thermal lesioning and may provide a superior binary test for lesioning. Meanwhile, the large and variable differences in segmented lesion sizes between intraoperative DWI and thermometry and post-operative T2-w imaging suggest that the DWI techniques presented here cannot reliably estimate the size of a lesion. The discrepancies in lesion sizes likely represent a combination of image artifacts, low resolution, and, potentially, unobserved evolution in the ADC of the lesion.

T-MRgFUS is being explored for new conditions such as neuropathic pain and epilepsy. Many of these procedures have targets that preclude the convenience of patient feedback. Treatment safety will heavily depend on accurate intraoperative monitoring. In these cases, reliable DWI may improve treatment safety and efficacy. Future work should address pertinent clinical questions such as whether DWI and ADC lesion contrasts remain stable over the first 24 hours after ablation and whether a tissue diffusion model can predict tremor reduction or adverse events.

One limitation to our study was variable image quality. For example, the variations in z-scores in Figures 6-7 appear to be too large to detect evolution in the ADC as a function of temperature, thermal dose, or time after ablation. Individually tuning the reconstruction algorithm for each imaging session may have implicitly biased the resulting images in favor of our hypothesis. Supporting Information Figure S1 indicates that the estimated ADC remains stable only within certain bands of the reconstruction parameters. Meanwhile, intraoperative diffusion imaging is inherently difficult. Improved acquisition schemes or scanner calibration methods are likely necessary to improve image quality. Priority developments include improving B1 transmit and reception (50) and mitigating the cascading effects of the large coupling water bath (36,51-53). These advances will be especially important during clinical procedures, which, when employing 3T scanners, currently lack custom coils.

The sonication methods employed in this study comprise a second limitation. The heating trajectory observed during each sonication was determined by the sonication parameters, the acoustic window, and intrinsic thermal diffusion and perfusion properties. As a result, some targets required the operator to attempt several sonications before finding the right pulsing parameters to achieve a peak observed temperature of at least 60 °C. Because the relationships between the diffusion tensor model and peak temperature and thermal dose are unknown, it is possible that multiple sonications during the treatment phase introduced variable DW and T2 evolution patterns relative to the monitoring time points. A more controlled sonication scheme would eliminate this potential source of data variability.

Conclusion

This paper presents a preclinical study of intraoperative DWI of thermal lesions. We find that DW imaging can visualize thermal lesions within 10 minutes of ablation and that lesion morphology and location remain consistent with post-operative imaging. T-MRgFUS lesions present a rapid and persistent decrease in ADC within minutes after ablation.

Supplementary Material

Refer to Web version on PubMed Central for supplementary material.

Acknowledgements

The authors express their gratitude to Drs. Ron Watkins and G. Wilson Miller for their assistance in RF coil design and construction.

This study was supported by the Focused Ultrasound Foundation, the University of Virginia Focused Ultrasound Center, NIH T32 HL 007284, and NIH R01 EB028773-01A1.

References

1. Lipsman N, Mainprize TG, Schwartz ML, Hynynen K, Lozano AM. Intracranial applications of magnetic resonance-guided focused ultrasound. Neurotherapeutics 2014;11:593–605. doi: 10.1007/s13311-014-0281-2. [PubMed: 24850310]
2. Elias WJ, Huss D, Voss T, et al. A pilot study of focused ultrasound thalamotomy for essential tremor. N. Engl. J. Med 2013;369. doi: 10.1056/NEJMoa1300962.
3. Ghanouni P, Pauly KB, Elias WJ, Henderson J, Sheehan J, Monteith S, Wintermark M. Transcranial MRI-Guided Focused Ultrasound: A Review of the Technologic and Neurologic Applications. Am. J. Roentgenol 2015;205:150–159. doi: 10.2214/AJR.14.13632. [PubMed: 26102394]
4. Lipsman N, Schwartz ML, Huang Y, Lee L, Sankar T, Chapman M, Hynynen K, Lozano AM. MR-guided focused ultrasound thalamotomy for essential tremor: A proof-of-concept study. Lancet. Neurol 2013;12:462–8. doi: 10.1016/S1474-4422(13)70048-6. [PubMed: 23523144]
5. Elias WJ, Lipsman N, Ondo WG, et al. A Randomized Trial of Focused Ultrasound Thalamotomy for Essential Tremor. N. Engl. J. Med 2016;375:730–739. doi: 10.1056/NEJMoa1600159. [PubMed: 27557301]
6. Li C, Gajic-Veljanoski O, Schaink AK, Higgins C, Fasano A, Sikich N, Dhalla I, Ng V. Cost-Effectiveness of Magnetic Resonance-Guided Focused Ultrasound for Essential Tremor. Mov. Disord 2018:1–9. doi: 10.1002/mds.27587. [PubMed: 29330922]
7. Ravikumar VK, Parker JJ, Hornbeck TS, Santini VE, Pauly KB, Wintermark M, Ghanouni P, Stein SC, Halpern CH. Cost-effectiveness of focused ultrasound, radiosurgery, and DBS for essential tremor. Mov. Disord 2017;32:1165–1173. doi: 10.1002/mds.26997. [PubMed: 28370272]
8. Boutet A, Ranjan M, Zhong J, et al. Focused ultrasound thalamotomy location determines clinical benefits in patients with essential tremor. Brain 2018;141:3405–3414. doi: 10.1093/brain/awy278. [PubMed: 30452554]
9. Cohen-Inbar O, Snell J, Xu Z, Sheehan J. What Holds Focused Ultrasound Back? World Neurosurg. 2016;91:661–665. doi: 10.1016/j.wneu.2016.04.007. [PubMed: 27432649]
10. Chen L, Bouley DM, Harris BT, Butts K. MRI study of immediate cell viability in focused ultrasound lesions in the rabbit brain. J. Magn. Reson. Imaging 2001;13:23–30. doi: 10.1002/1522-2586(200101)13:1<23::AID-JMRI1004>3.0.CO;2-G. [PubMed: 11169799]
11. Hynynen K, Vykhodtseva NI, Chung AH, Sorrentino V, Colucci V, Jolesz FA. Thermal effects of focused ultrasound on the brain: determination with MR imaging. Radiology 1997;204:247–53. doi: 10.1148/radiology.204.1.9205255. [PubMed: 9205255]

12. Wintermark M, Druzgal J, Huss DS, et al. Imaging findings in MR imaging-guided focused ultrasound treatment for patients with essential tremor. AJNR. Am. J. Neuroradiol 2014;35:891–6. doi: 10.3174/ajnr.A3808. [PubMed: 24371027]
13. Huang Y, Lipsman N, Schwartz ML, Krishna V, Sammartino F, Lozano AM, Hynynen K. Predicting lesion size by accumulated thermal dose in MR-guided focused ultrasound for essential tremor. Med. Phys 2018;45:4704–4710. doi: 10.1002/mp.13126. [PubMed: 30098027]
14. Breen MS, Breen M, Butts K, Chen L, Saidel GM, Wilson DL. MRI-guided thermal ablation therapy: Model and parameter estimates to predict cell death from MR thermometry images. Ann. Biomed. Eng 2007;35:1391–1403. doi: 10.1007/s10439-007-9300-3. [PubMed: 17436111]
15. McDannold N, Vykhodtseva N, Jolesz FA, Hynynen K. MRI Investigation of the Threshold for Thermally Induced Blood-Brain Barrier Disruption and Brain Tissue Damage in the Rabbit Brain. Magn. Reson. Med 2004;51:913–923. doi: 10.1002/mrm.20060. [PubMed: 15122673]
16. Chung AH, Jolesz FA, Hynynen K. Thermal dosimetry of a focused ultrasound beam in vivo by magnetic resonance imaging. Med. Phys 1999;26:2017–2026. doi: 10.1118/1.598707. [PubMed: 10505893]
17. Bond AE, Elias WJ. Predicting lesion size during focused ultrasound thalamotomy: a review of 63 lesions over 3 clinical trials. Neurosurg. Focus 2018;44:E5. doi: 10.3171/2017.11.FOCUS17623.
18. Chen L, Bouley D, Yuh E, D'Arceuil H, Butts K. Study of focused ultrasound tissue damage using MRI and histology. J. Magn. Reson. imaging 1999;10:146–153. doi: 10.1002/(sici)1522-2586(199908)10:2<146::aid-jmri6>3.0.co;2-c. [PubMed: 10441017]
19. Mórocz IÁ, Hynynen K, Gudbjartsson H, Peled S, Colucci V, Jólesz FA. Brain edema development after MRI-guided focused ultrasound treatment. J. Magn. Reson. Imaging 1998;8:136–142. doi: 10.1002/jmri.1880080126. [PubMed: 9500273]
20. Vykhodtseva N, Sorrentino V, Jolesz FA, Bronson RT, Hynynen K. MRI detection of the thermal effects of focused ultrasound on the brain. Ultrasound Med. Biol 2000;26:871–80. doi: 10.1016/S0301-5629(00)00216-7. [PubMed: 10942834]
21. Vykhodtseva N, Mcdannold N, Martin H, Bronson RT, Hynynen K. Apoptosis in ultrasound-produced threshold lesions in the rabbit brain. Ultrasound Med. Biol 2001;27:111–117. doi: 10.1016/S0301-5629(00)00275-1. [PubMed: 11295277]
22. Pilatou MC, Stewart EA, Maier SE, Fennessy FM, Hynynen K, Tempany CMC, McDannold N. MRI-based thermal dosimetry and diffusion-weighted imaging of MRI-guided focused ultrasound thermal ablation of uterine fibroids. J. Magn. Reson. Imaging 2009;29:404–11. doi: 10.1002/jmri.21688. [PubMed: 19161196]
23. Jacobs MA, Herskovits EH, Kim HS. Uterine fibroids: diffusion-weighted MR imaging for monitoring therapy with focused ultrasound surgery--preliminary study. Radiology 2005;236:196–203. doi: 10.1148/radiol.2361040312. [PubMed: 15987974]
24. Chen J, Daniel BL, Diederich CJ, Bouley DM, Van Den Bosch MAAJ, Kinsey AM, Sommer G, Pauly KB. Monitoring prostate thermal therapy with diffusion-weighted MRI. Magn. Reson. Med 2008;59:1365–1372. doi: 10.1002/mrm.21589. [PubMed: 18506801]
25. Cheng HLM, Haider MA, Dill-Macky MJ, Sweet JM, Trachtenberg J, Gertner MR. MRI and contrast-enhanced ultrasound monitoring of prostate microwave focal thermal therapy: An in vivo canine study. J. Magn. Reson. Imaging 2008;28:136–143. doi: 10.1002/jmri.21415. [PubMed: 18581405]
26. Martin E, Jeanmonod D, Morel A, Zadicario E, Werner B. High-intensity focused ultrasound for noninvasive functional neurosurgery. Ann. Neurol 2009;66:858–61. doi: 10.1002/ana.21801. [PubMed: 20033983]
27. Sammartino F, Yeh F-C, Krishna V. Longitudinal analysis of structural changes following unilateral focused ultrasound thalamotomy. NeuroImage. Clin 2019;22:101754. doi: 10.1016/j.nicl.2019.101754. [PubMed: 30921612]
28. Jung HH, Chang WS, Rachmilevitch I, Tlusty T, Zadicario E, Chang JW. Different magnetic resonance imaging patterns after transcranial magnetic resonance-guided focused ultrasound of the ventral intermediate nucleus of the thalamus and anterior limb of the internal capsule in patients with essential tremor or obsessive-comp. J. Neurosurg 2015;122:162–8. doi: 10.3171/2014.8.JNS132603. [PubMed: 25343176]

29. Wintermark M, Huss DS, Shah BB, Tustison N, Druzgal TJ, Kassell N, Elias WJ. Thalamic connectivity in patients with essential tremor treated with MR imaging-guided focused ultrasound: in vivo fiber tracking by using diffusion-tensor MR imaging. Radiology 2014;272:202–9. doi: 10.1148/radiol.14132112. [PubMed: 24620914]
30. Mazerolle E, Warwaruk-Rogers R, Sevick R, Sankar T, Pichardo S, Zaaroor M, Martino D, Kiss Z, Pike G. MR-guided focused ultrasound for essential tremor: Initial MRI observations. In: 6th International Symposium on Focused Ultrasound. Reston, VA; 2018.
31. Plata JC, Holbrook AB, Marx M, et al. A feasibility study on monitoring the evolution of apparent diffusion coefficient decrease during thermal ablation. Med. Phys 2015;42:5130–5137. doi: 10.1118/1.4928155. [PubMed: 26328964]
32. Chazen JL, Stradford T, Kaplitt MG. Cranial MR-guided Focused Ultrasound for Essential Tremor. Clin. Neuroradiol 2019;29:351–357. doi: 10.1007/s00062-018-0709-x. [PubMed: 30046918]
33. Elias WJ, Khaled M, Hilliard JD, Aubry JF, Frysinger RC, Sheehan JP, Wintermark M, Lopes MB. A magnetic resonance imaging, histological, and dose modeling comparison of focused ultrasound, radiofrequency, and Gamma Knife radiosurgery lesions in swine thalamus. J Neurosurg 2013;119:307–317. doi: 10.3171/2013.5.JNS122327. [PubMed: 23746105]
34. Félix B, Léger ME, Albe-Fessard D, Marcilloux JC, Rampin O, Laplace JP. Stereotaxic atlas of the pig brain. Brain Res. Bull 1999;49:1–137. [PubMed: 10466025]
35. Lechner-Greite SM, Hehn N, Werner B, Zadicario E, Tarasek M, Yeo D. Minimizing eddy currents induced in the ground plane of a large phased-array ultrasound applicator for echo-planar imaging-based MR thermometry. J. Ther. ultrasound 2016;4:4. doi: 10.1186/s40349-016-0047-x. [PubMed: 26848391]
36. Allen SP, Steeves T, Fergusson A, Moore D, Davis RM, Vlaisialjevich E, Meyer CH. Novel acoustic coupling bath using magnetite nanoparticles for MR-guided transcranial focused ultrasound surgery. Med. Phys 2019;46:5444–5453. doi: 10.1002/mp.13863. [PubMed: 31605643]
37. Auerbach E, Ugurbil K. Improvement in Diffusion MRI at 3T and Beyond with the Twice-Refocused Adiabatic Spin Echo (TRASE) Sequence. In: Proceedings of the 12th Annual Meeting of ISMRM. ; 2004. p. 2464.
38. Skare S, Balchandani P, Newbould R, Bammer R. Adiabatic refocusing pulses in 3T and 7T diffusion imaging. In: Proceedings of the 15th Annual Meeting of ISMRM. ; 2007. p. 1493.
39. Conolly S, Glover G, Nishimura D, Macovski A. A reduced power selective adiabatic spin-echo pulse sequence. Magn. Reson. Med 1991;18:28–38. doi: 10.1002/2014GB005021. [PubMed: 2062239]
40. Liu C, Bammer R, Kim DH, Moseley ME. Self-navigated interleaved spiral (SNAILS): Application to high-resolution diffusion tensor imaging. Magn. Reson. Med 2004;52:1388–1396. doi: 10.1002/mrm.20288. [PubMed: 15562493]
41. Fielden SW, Meyer CH. A simple acquisition strategy to avoid off-resonance blurring in spiral imaging with redundant spiral-in/out k-space trajectories. Magn. Reson. Med 2015;73:704–710. doi: 10.1002/mrm.25172. [PubMed: 24604539]
42. Allen SP, Feng X, Fielden SW, Meyer CH. Correcting image blur in spiral, retraced in/out (RIO) acquisitions using a maximized energy objective. Magn. Reson. Med 2019;81:1806–1817. doi: 10.1002/mrm.27541. [PubMed: 30421451]
43. Reese TG, Heid O, Weisskoff RMM, Wedeen VJJ. Reduction of eddy-current-induced distortion in diffusion MRI using a twice-refocused spin echo. Magn. Reson. Med 2003;49:177–82. doi: 10.1002/mrm.10308. [PubMed: 12509835]
44. Meyer CH, Pauly JM, Macovski A, Nishimura DG. Simultaneous spatial and spectral selective excitation. Magn. Reson. Med 1990;15:287–304. [PubMed: 2392053]
45. Mugler JP. Optimized three-dimensional fast-spin-echo MRI. J. Magn. Reson. Imaging 2014;39:745–767. doi: 10.1002/jmri.24542. [PubMed: 24399498]
46. Jackson JI, Meyer CH, Nishimura DG, Macovski A. Selection of a convolution function for Fourier inversion using gridding (computerised tomography application). IEEE Trans. Med. Imaging 1991;10:473–478. doi: 10.1109/42.97598. [PubMed: 18222850]

47. Liu C, Moseley ME, Bammer R. Simultaneous phase correction and SENSE reconstruction for navigated multi-shot DWI with non-cartesian k-space sampling. Magn. Reson. Med 2005;54:1412–22. doi: 10.1002/mrm.20706. [PubMed: 16276497]

48. Gudbjartsson H, Patz S. The rician distribution of noisy mri data. Magn. Reson. Med 1995;34:910–914. doi: 10.1002/mrm.1910340618. [PubMed: 8598820]

49. Miller AJ, Joseph PM. The use of power images to perform quantitative analysis on low SNR MR images. Magn. Reson. Imaging 1993;11:1051–1056. doi: 10.1016/0730-725X(93)90225-3. [PubMed: 8231670]

50. Hadley JR, Odeen H, Merrill R, Haag-Roeger R, Rieke V, Payne A, Parker DL. Improving Image Quality in Transcranial Magnetic Resonance Guided Focused Ultrasound Using a Copper Screen. In: Cleveland RO, Khokhlova VA, editors. Abstract Book of 19th International Symposium for Therapeutic Ultrasound. Barcelona; 2019. p. 33.

51. Odeen H, Rieke V, Patil S, Bolster BD, Bhat H, Parker DL. Volumetric MR thermometry for neuro applications using multiple 3D slabs and saturation bands. In: Cleveland RO, Khokhlova VA, editors. Abstract Book of 19th International Symposium for Therapeutic Ultrasound. Barcelona; 2019. p. 36.

52. Grissom WA, Allen S. Reducing temperature errors in transcranial MR-guided focused ultrasound using a reduced-field-of-view sequence. Magn. Reson. Med 2020;83:1016–1024. doi: 10.1002/mrm.27987. [PubMed: 31483525]

53. Deckers R, Merckel LG, Denis de Senneville B, Schubert G, Köhler M, Knuttel FM, Mali WPTM, Moonen CTW, van den Bosch MAAJ, Bartels LW. Performance analysis of a dedicated breast MR-HIFU system for tumor ablation in breast cancer patients. Phys. Med. Biol 2015;60:5527–42. doi: 10.1088/0031-9155/60/14/5527. [PubMed: 26133986]

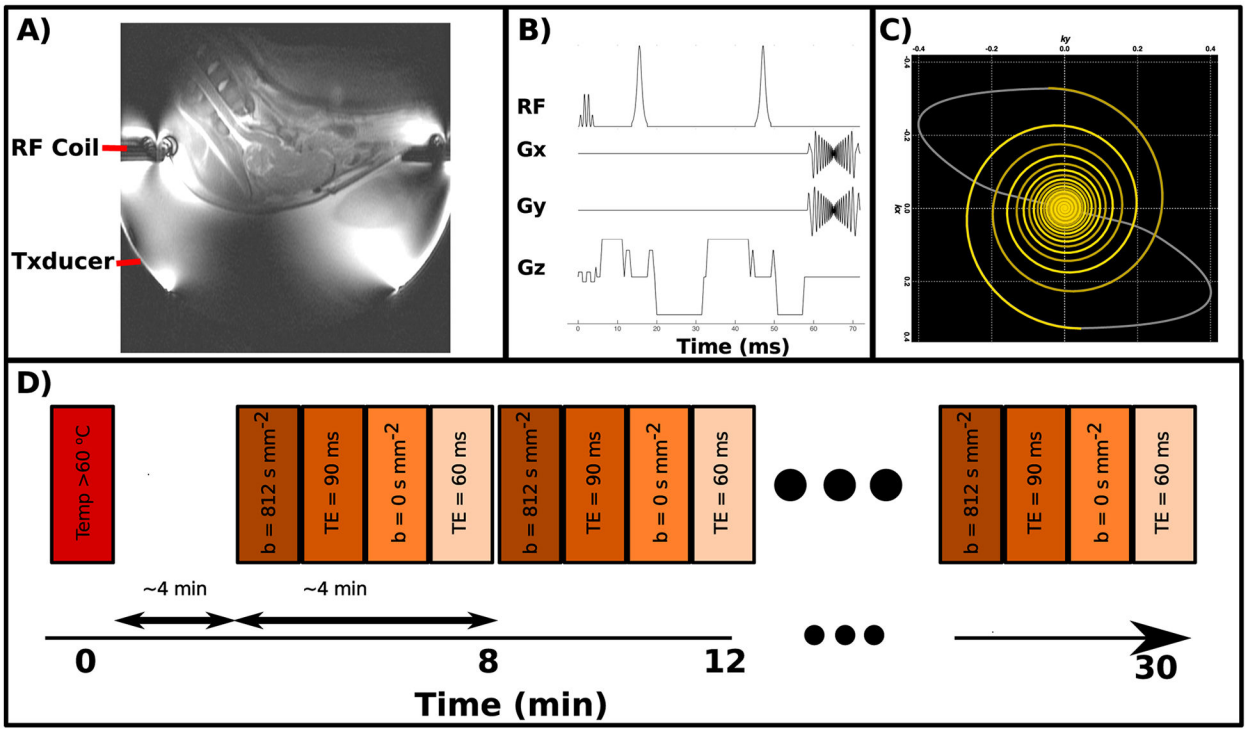

Figure 1:

A) Image of the experimental setup with the RF coil and transducer indicated **B)** Diagram of the custom, multi-shot pulse sequence. **C)** Plot of the retraced, variable density spiral trajectory used in this sequence. **D)** Timing diagram of the series of imaging techniques used to monitor lesion development after ablation. Each colored bar represents a separate imaging sequence.

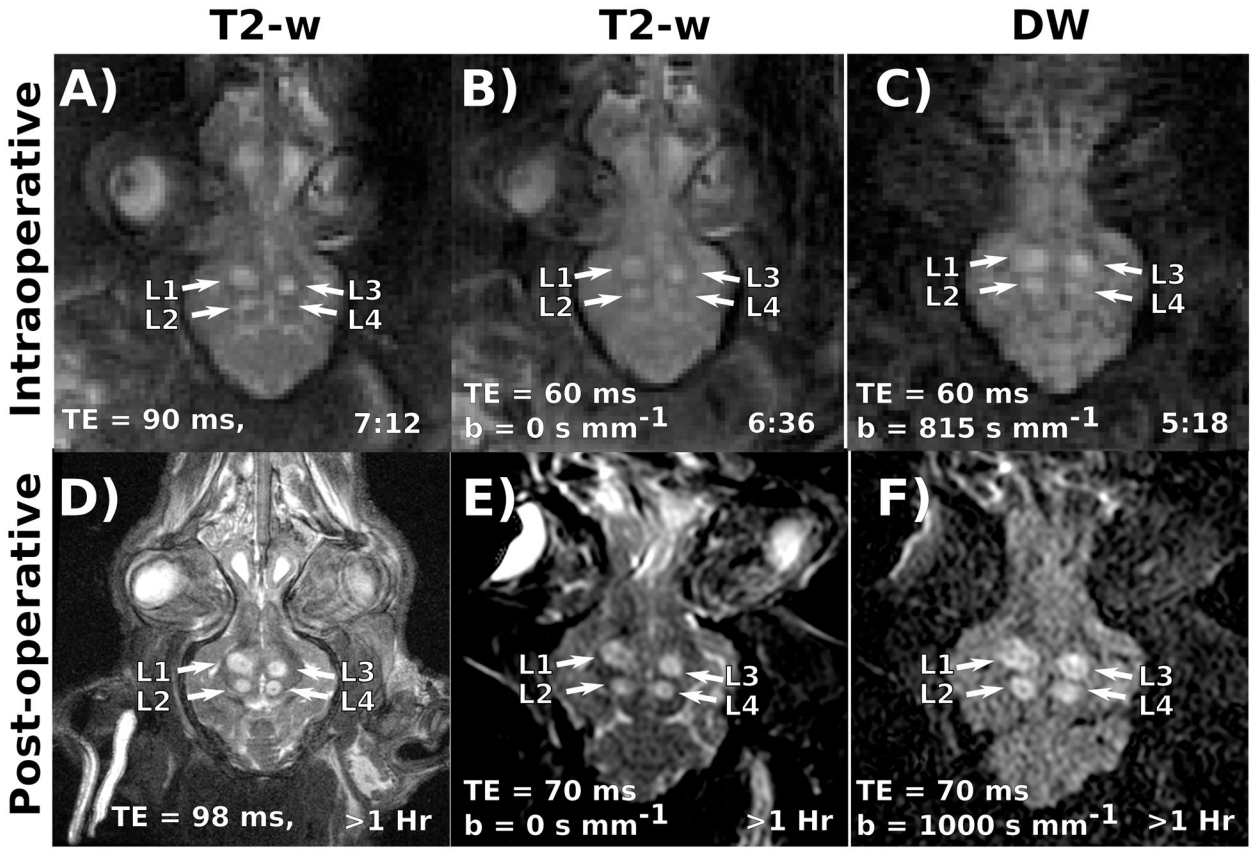

Figure 2:

(**Top Row**) Example Intraoperative T2-w (**A, B**), and diffusion-weighted images (**C)** in subject 5. Relevant contrast parameters and the time elapsed since ablating the fourth and final target are also displayed. Three lesions (labeled L1-3) demonstrate well developed T2-w contrast. However, L4 appears much more readily on the DW image. (**Bottom Row**) Example post-operative T2-w (**D, E**), and diffusion-weighted images (**F**) images of the same animal. Relevant contrast parameters and the time elapsed since ablating the fourth and final target are also displayed. By this point, all lesions have had time to develop T2-w contrast. Post-operative lesion morphology matches well with the intraoperative images.

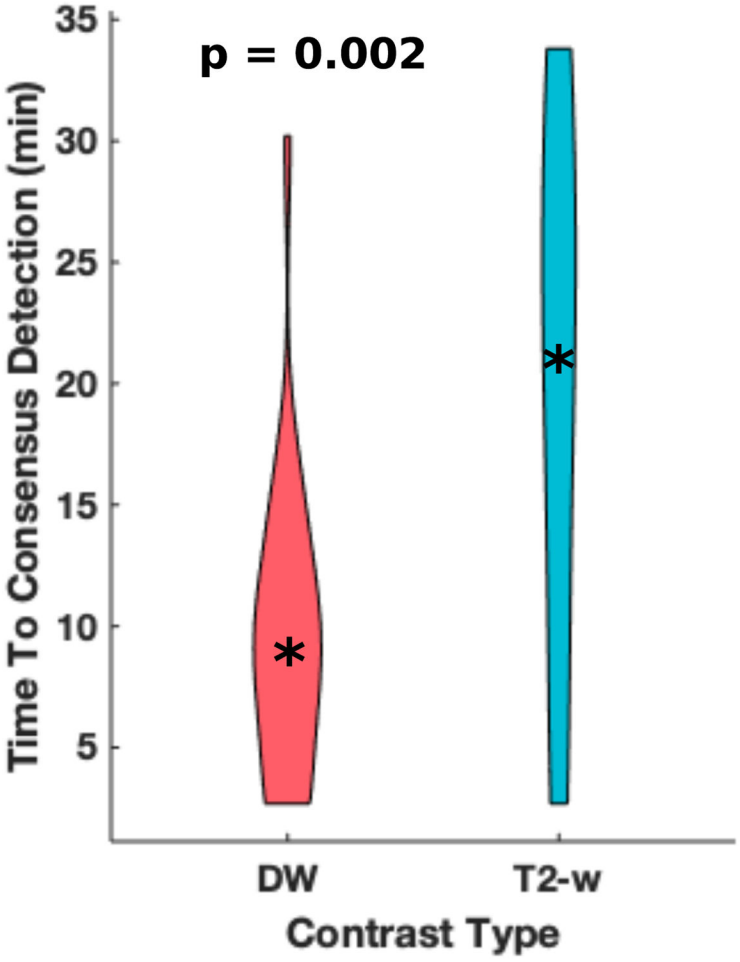

Figure 3:
Violin plots (with a point marking the median value) of the observed times to consensus detection by image reviewers. On average, lesions observed on DW images produced earlier times to consensus detection. For lesions observed on DW images, the 0.25 and 0.75 quantiles of consensus detection times are 3.6 and 11.8 minutes. Meanwhile, for lesions observed on T2-w images, the 0.25 and 0.75 quantiles of consensus detection times are 10.6 and 27.8 minutes.

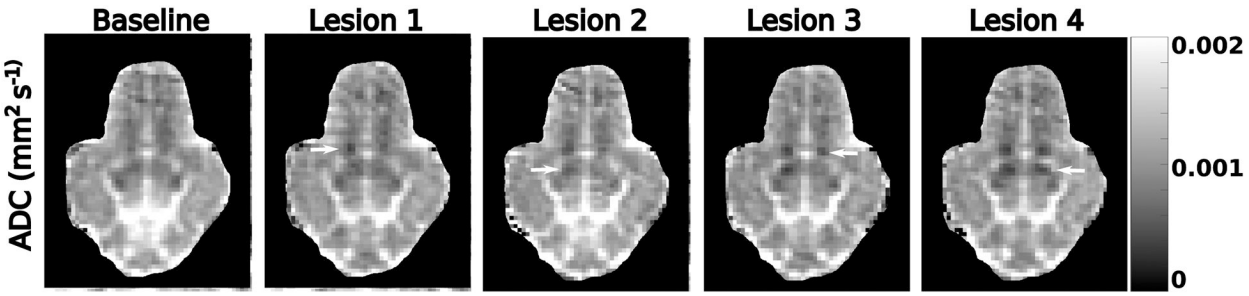

Figure 4:

ADC maps from subject 6 acquired during the monitoring sessions corresponding to the labels above each column. Lesion locations are indicated by the white arrows. For lesions 1-4, the ADC maps were acquired within 10 minutes of ablation. Lesions 1 and 4 display a strong decrease in ADC immediately after ablation. For clarity, the noisy background of each ADC image has been artificially masked.

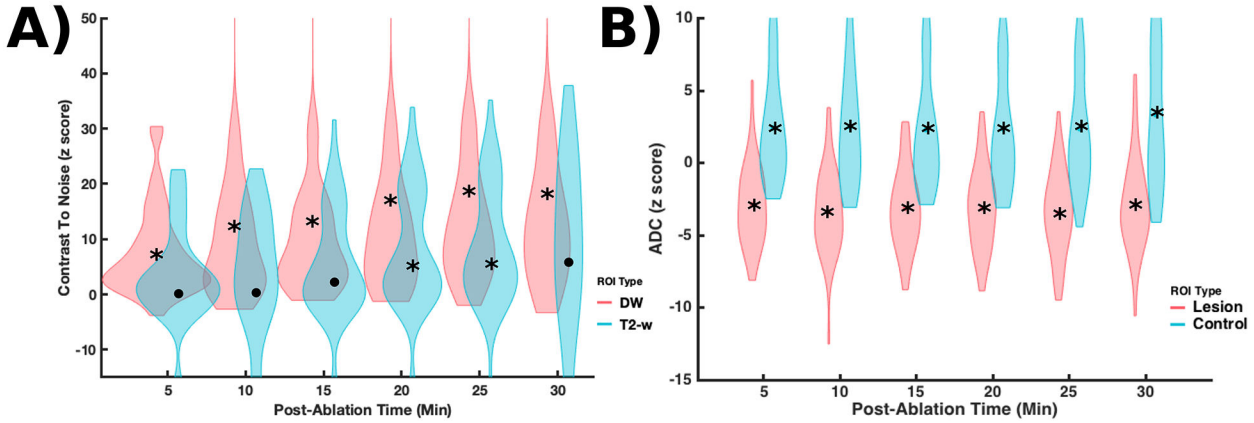

Figure 5:

(**A**) Violin plots (with a point marking the median value) of T2-w and DW z-scores binned in 5-minute increments after ablation for all lesion ROI's. A z-score of zero indicates no change T2-w or DW image magnitude between baseline and treatment monitoring sessions. The majority of DW z-scores show more pronounced contrast after ablation. (**B**) Violin plots (with a point marking the median value) of ADC z-scores binned in 5-minute increments for both lesion and control ROI's. Medians marked by an asterisk represent statistically significant z-scores at the 0.0083 level. The majority of lesions display a large and sustained decrease in ADC values after ablation relative to the estimated standard deviation of the measurement. The control ROI's display a slight increase in ADC between the baseline and treatment monitoring sessions, which may be either physiologic or a result of residual scanner drift.

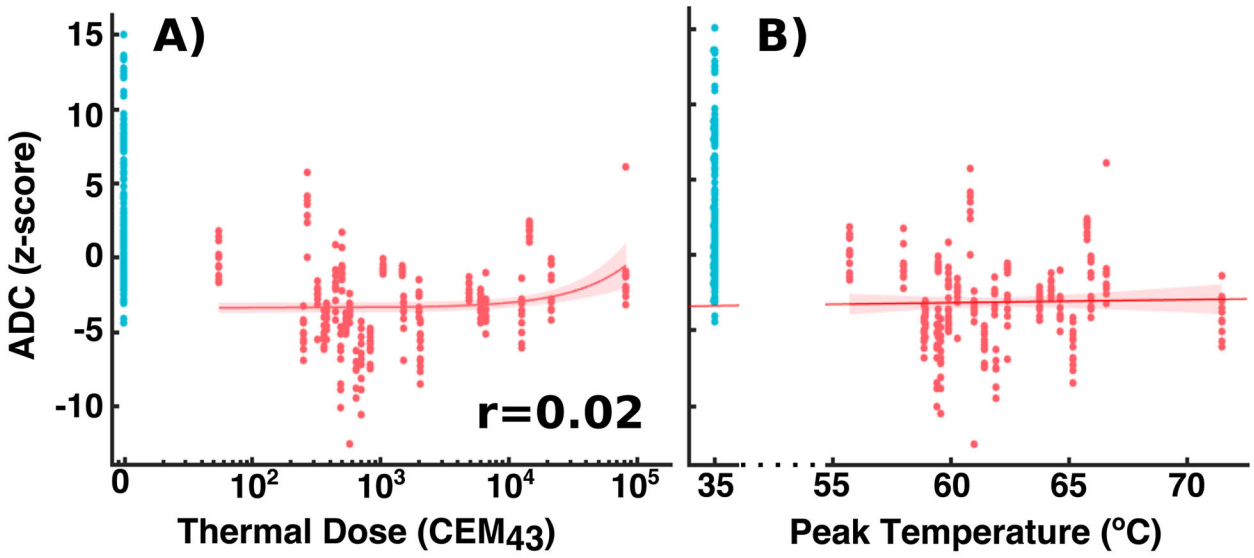

Figure 6:

(A) The ADC z-scores for all the ROI's used for ROC analysis as a function of (**A**) observed thermal dose (note the log scale of the *x* axis) and (**B**) observed peak temperature. Untreated targets are colored blue for easier visibility. The plots also display least-squares linear fits of the z scores with accompanying 95% confidence bounds and Pearson correlation coefficients. Treated and un-treated ROI's show differentiated populations. However, the variation in z-scores between treated ROI's appears too large to capture variations in ADC as a function of thermal dose or peak temperature.

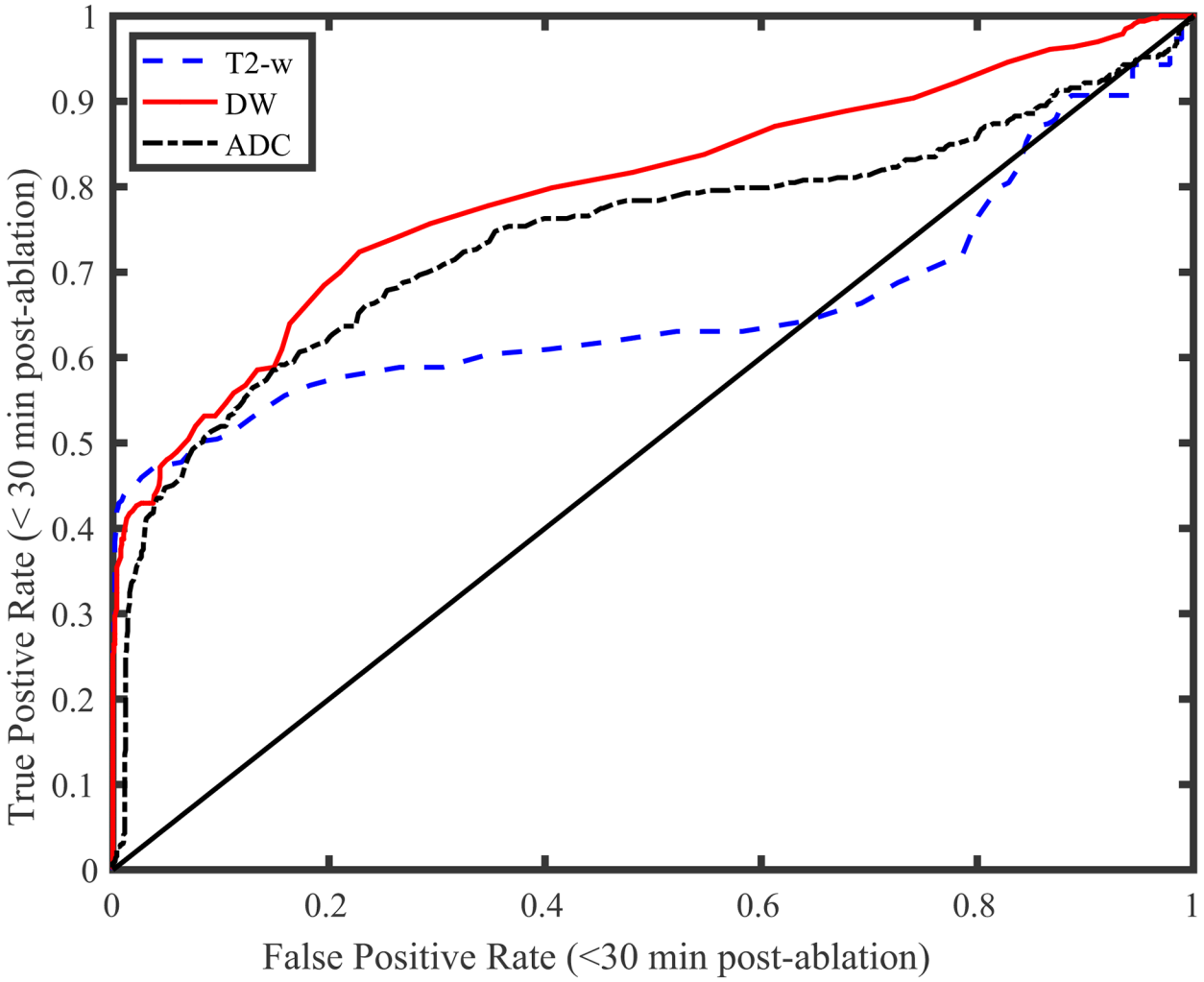

Figure 7:

Lesion detection ROC curves for several T2-w, DW, and ADC z score thresholds. These threshold were used to classify treated and untreated targets imaged within 35 minutes of treatment. The DW and ADC curves present nearly identical areas (0.69 and 0.68, respectively) while the T2-w curve presents an area of 0.49. The minimum distances to the upper left corners of the plot were 0.58, 0.41, and 0.55 for the T2-w, DW, and ADC z-scores, respectively.

Table 1:

Description of the number of animal models used, the number of lesions formed within each animal and relevant metrics associated with each lesion such as number of sonications per lesion, peak temperature, total energy deposited into the animal, total thermal dose, and lesion area (estimated from in-plane thermometry).

Subject #	Lesion #	# of Sonications	Total Energy (kJ)	Peak Temperature (C)	Thermal Dose (CEM 240)	Dose Area (mm2)
1	1	6	0.0	60.8	267	6.0
	2	7	0.0	62.4	1481	8.4
	3	3	0.0	61.0	582	6.0
	4	5	0.0	60.3	323	4.8
2	1	11	0.0	59.4	498	7.2
	2	8	0.0	61.9	656	8.4
	3	7	0.0	62.4	1522	9.6
	4	8	0.0	61.9	1996	12.0
3	1	5	0.0	58.9	252	6.0
	2	7	0.0	59.9	445	9.6
	3	6	0.0	59.5	368	7.2
	4	7	0.0	64.2	4932	9.6
	5	4	0.0	61.4	842	7.2
4	1	5	0.0	55.7	383	7.2
	2	3	0.0	61.1	14655	15.6
	3	4	0.0	59.7	6130	14.4
	4	2	0.0	56.4	537	9.6
	5	1	0.0	61.0	12888	13.2
5	1	5	0.0	66.6	83202	190.2
	2	5	0.0	58.0	506	20.3
	3	4	0.0	60.4	705	9.6
6	1	4	0.0	65.2	2047	9.6
	2	4	0.0	66.0	21756	12.0
	3	3	0.0	64.7	6705	12.0
	4	4	0.0	59.6	715	8.4

Table 2:

MRI parameters used to observe diffusion image contrast during the experiment. Some parameters were varied between each experiment to explore tradeoffs between resolution, SNR, and navigator coverage.

Pig	TE/TR	Slice Thickness / Slice Gaps / # slices	resolution / matrix size	Spiral Interleaves / Readout Duration	Image Acqusition Time	b values	a/b/f
1	60 ms\ 1.5 s	5 mm \ 1 mm \ 3	1 mm / 300 x 300	64 / 11 ms	192 (s)	0, 815 (s mm^{-2})	30/0.5/−50
2	60 ms\ 1.5 s	5 mm\ 1 mm \ 3	1 mm / 300 x 300	64 / 11 ms	192 (s)	0, 815 (s mm^{-2})	30/0.5/−50
3	60 ms\ 1.5 s	7 mm\ 1 mm \ 3	1.8 mm / 168 x 168	32 / 11 ms	96 (s)	0, 815 (s mm^{-2})	30/0.5/−42
4	60 ms\ 1.5 s	7 mm\ 1 mm \ 3	1.5 mm / 200 x 200	44 / 11 ms	132 (s)	0, 815 (s mm^{-2})	30/0.5/−44.5
5	60 ms\ 1.5 s	7 mm\ 1 mm \ 3	1.5 mm / 200 x 200	52 / 11 ms	156 (s)	0, 815 (s mm^{-2})	30/0.5/−44.5
6	60 ms\ 1.5 s	7 mm \ 1 mm \ 3	1.5 mm / 200 x 200	52/ 11 ms	156 (s)	0, 815 (s mm^{-2})	30/0.5/−44.5